small
NANO MICRO
www.small-journal.com

Passive Picoinjection Enables Controlled Crystallization in a Droplet Microfluidic Device

Shunbo Li, Muling Zeng, Thembaninkosi Gaule, Michael J. McPherson, and Fiona C. Meldrum**

Segmented flow microfluidic devices offer an attractive means of studying crystallization processes. However, while they are widely employed for protein crystallization, there are few examples of their use for sparingly soluble compounds due to problems with rapid device fouling and irreproducibility over longer run-times. This article presents a microfluidic device which overcomes these issues, as this is constructed around a novel design of "picoinjector" that facilitates direct injection into flowing droplets. Exploiting a Venturi junction to reduce the pressure within the droplet, it is shown that passive injection of solution from a side-capillary can be achieved in the absence of an applied electric field. The operation of this device is demonstrated for calcium carbonate, where highly reproducible results are obtained over long run-times at high supersaturations. This compares with conventional devices that use a Y-junction to achieve solution loading, where in-channel precipitation of calcium carbonate occurs even at low supersaturations. This work not only opens the door to the use of microfluidics to study the crystallization of low solubility compounds, but the simple design of a passive picoinjector will find wide utility in areas including multistep reactions and investigation of reaction dynamics.

1. Introduction

Microdroplets provide excellent environments for performing and studying crystallization processes. While crystallization in bulk solution is often affected by impurities, the vessel surface, and the inhomogeneities in solution composition that occur during mixing, droplets offer highly reproducible reaction volumes.[1] In addition, they only require small quantities of reagents and multiple droplets can be created and screened in parallel, enabling large data-sets to be generated for statistical analysis. One of the most convenient ways of generating large numbers of identical droplets is using microfluidic devices.[2] These can be used to create static arrays and continuously flowing droplets, and a wide range of techniques are available for on-chip analysis.[3,4] Microfluidic systems are therefore attracting increasing attention for applications such as studying nucleation kinetics,[5,6] for screening protein crystallization conditions and generating large protein crystals for structural analysis,[7–9] and for exploring polymorphism in organic[10,11] and inorganic crystal systems.[12–14]

A range of strategies have been used to achieve on-chip crystallization. Protein crystals are often highly soluble such that precipitation can be effectively achieved by combining protein and precipitant solutions at the point of droplet formation,[6,8] or controlling water removal from the plugs of protein solution.[15] More complex strategies have also been explored to promote the formation of high quality crystals including valve-based systems,[9,16] merging of alternate droplets containing protein and precipitant, and separation of nucleation and growth events,[17] where additional protein/ precipitant is added to existing plugs downstream of the point of initial droplet formation. Crystallization of soluble organics and inorganics has also been achieved via droplet-shrinkage[18] and on-chip temperature control.[11,13]

Many crystal systems that are important to industry, the environment, and biology—such as calcium carbonate, sulfate, and phosphate—are highly insoluble, however, which results in short induction times and makes on-chip study of their precipitation more challenging due to problems with device fouling.[12] While precipitation within droplets rather than single-phase systems greatly reduces channel fouling,[19] the formation of supersaturated droplets by combining cation and anion solutions using a conventional "Y-shaped" channel or equivalent inevitably leads to precipitation at this junction. This can give rise to a range of problems including the introduction of crystal seeds into droplets. These issues can be minimized, or even eliminated, using droplet fusion—where pairs of droplets are fused using special channel architectures or applied fields[20]—or direct injection strategies, where use of a "picoinjector" to add solution to flowing droplets[21,22] offers

Dr. S. Li, Dr. M. Zeng, Prof. F. C. Meldrum
School of Chemistry
University of Leeds
Leeds LS2 9JT, UK
E-mail: chmslic@leeds.ac.uk; f.meldrum@leeds.ac.uk
Dr. T. Gaule, Prof. M. J. McPherson
Astbury Centre for Structural Molecular Biology
School of Molecular and Cellular Biology
University of Leeds
Leeds LS2 9JT, UK

DOI: 10.1002/smll.201702154

short contact times and avoids problems of channel fouling. However, droplet fusion relies on excellent control over flow rates to ensure that the droplet streams are perfectly ordered prior to coalescence,[23] while picoinjector devices are typically complex to construct, requiring an applied electric field to achieve injection.[21,24]

Here, we present a microfluidic device design that enables reliable, on-chip analysis of the precipitation of insoluble crystals in flowing droplets. At the heart of our device is a simple design of picoinjector that employs a Venturi junction to achieve injection into surfactant-stabilized droplets. Effective control over the volume injected is achieved by variation of the flow rates. This device is then used to precipitate calcium carbonate within droplets, where a serpentine channel located after the injector zone ensures essential effective mixing of the cation and anion solutions. Comparison with the use of a Y-junction to mix anion and cation solutions at the point of droplet-formation demonstrates the flaws of this traditional design, and shows how our new chip design eliminates all problems of channel fouling and ensures that crystallization occurs uniquely within droplets. Our device design—and the insight gained into the precipitation of insoluble inorganics on-chip—will therefore enable researchers to profit from segmented flow microfluidic devices to study crystallization mechanisms, and ultimately to learn how to control crystallization processes.

2. Results

The goal of our work was to explore microfluidic device designs that would enable the crystallization of insoluble compounds to be performed and studied in droplets under highly reproducible and reliable conditions. This was achieved by comparing the function of a simple Y-junction and a more complex picoinjector to create supersaturated solutions, and investigating the influence on the rate of mixing of solutions within the droplets. To achieve our aim it was also necessary to develop a novel design of picoinjector whose ease of operation would allow our device to be used by crystallization scientists rather than expert microfluidic labs. Calcium carbonate was used in our study due to its importance in biology, the environment, and industry. It also exhibits a rich polymorphism—amorphous calcium carbonate (ACC, $CaCO_3 \cdot H_2O$), vaterite, aragonite, and calcite can all be precipitated from solution at room temperature—and a wide range of morphologies. It is therefore widely used as a "test system" for studying and understanding the crystallization of insoluble inorganic compounds.[25]

2.1. Design and Construction of the Microfluidic Device

Our device was designed such that a single chip could be used to compare on-chip crystallization in droplets by creating a supersaturated solution (i) at the point of droplet formation and (ii) using a downstream picoinjector. The channel design is shown in **Figure 1**a, where zone 1 is designed for droplet generation using a T-junction, and the associated Y-shaped channel can be used to combine anion and cation solutions prior to droplet generation. Zone 2 features a Venturi junction where solution is injected into individual droplets via a narrow quartz capillary. This device also comprises serpentine channel to ensure effective mixing,[26] where the impact of this on the crystallization of calcium carbonate is discussed in detail in Section 2.5.

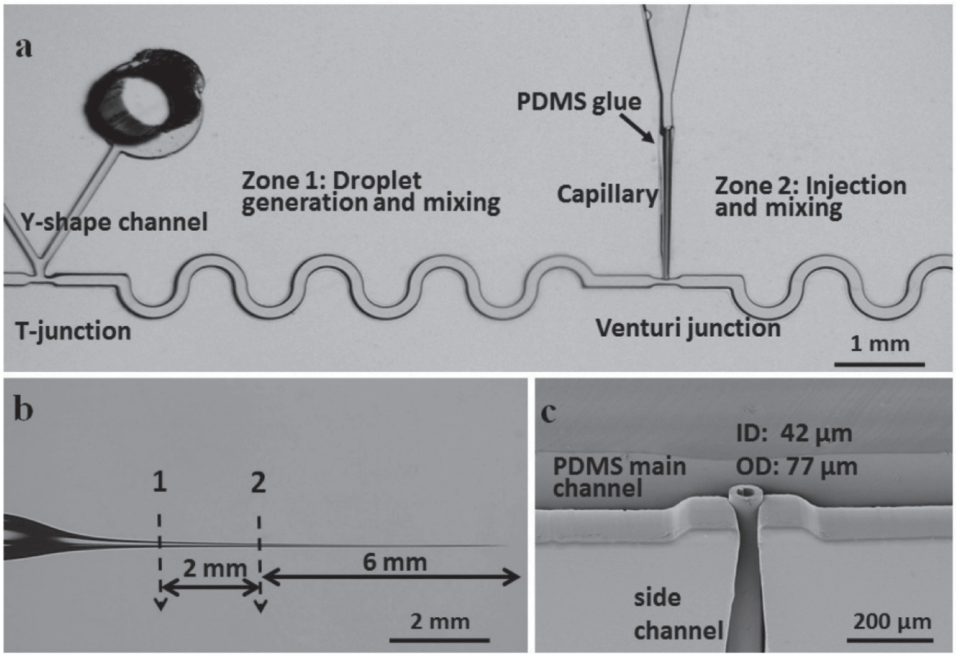

Figure 1. a) Design of microfluidic device, where droplet generation occurs in Zone 1, and injection occurs in Zone 2. b) Optical image of a quartz capillary, which is cut at 6 and 8 mm from the tip to give the 2 mm section inserted into the chip. c) SEM image showing how the capillary is located in a side channel in the Venturi junction.

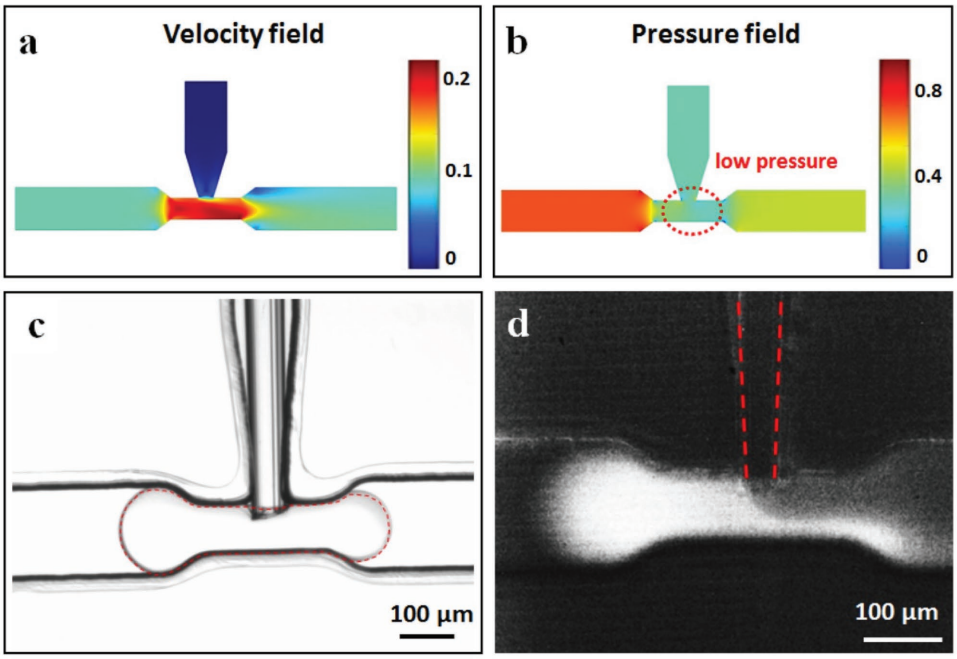

Figure 2. a) The velocity field and b) the pressure field associated with the Venturi junction, as modeled using COMSOL Multiphysics. c) Snapshot of a droplet (outlined by red dashed line) passing through the Venturi junction and d) the injection process of a fluorophore solution, as recorded with a high speed camera mounted on a fluorescence microscope. The capillary is outlined by red dashed lines to aid viewing.

Devices were fabricated from poly(dimethylsiloxane) (PDMS) using soft photolithographic techniques, where a side channel in the PDMS ensures the correct location of the capillary.[27] The PDMS channels have heights of 100 µm and widths of 150 µm, where these narrow to 75 µm at the T-junction and Venturi junction. Capillaries of dimensions i.d. 0.5 mm, o.d. 1 mm, and length 7.5 cm were pulled using a laser pipette puller, and subsequently cut into a 2 mm section (Figure 1b). An optical microscope was used to assist in the placement of the capillary section in the chip, which was glued in place using partially cured PDMS (baked at 60 °C for 20 min). A scanning electron microscope (SEM) image of the Venturi junction is shown in Figure 1c, where the outer dimension of the capillary is larger than the width of the PDMS side channel, but smaller than its height. The former feature helps in fixing the capillary in place.

2.2. Function of the Venturi Junction in the Picoinjector

Our channel design exploits the Venturi effect—which describes the reduction in fluid pressure that occurs when a fluid flows through a constricted section of a channel—to ensure that the moving droplets come into contact with the hydrophilic capillary.[28] Simulations of fluid flow through the Venturi junction of our device was performed using COMSOL based on a single phase laminar flow model. A 2D stationary model was adopted to simplify the calculations. The dimensions of the junction were taken from our device and the physical properties of the flowing fluid were those of FC-40. The simulations of the velocity field and pressure distribution of the Venturi junction are shown in **Figure 2**a,b. As expected, the velocity is greatly increased in the narrow junction in accordance with the principle of mass conservation, leading to a decrease in pressure according to the principle of conservation of mechanical energy (Figure 2b). The Venturi effect can therefore be exploited to decrease the pressure required in the side channel to inject fluid into the droplets, where high pressures can cause instability and tunneling between the capillary and PDMS side channel.

Successful injection also relies on the maintenance of a high pressure across the main and the side channel, where this is critical to achieving injection of a wide range of solution volumes, and in the prevention of secondary droplet formation at the capillary. The maximum pressure difference is governed by the Laplace pressure:

$$\Delta P_{\mathrm{L}} = 4\gamma/w \tag{1}$$

where, γ is the water/oil interfacial tension and w is the inner diameter of capillary, which is 42 µm in our device. The maximum pressure calculated using this equation is the pressure before, not during injection, where this is only valid when the capillary is rounded, such that spherical droplets are present. Taking the interfacial tension to be ≈10 mN m^{-1}, as previously measured for droplets stabilized by 0.5% (wt/wt) raindance surfactant,[29] the injector can maintain a maximum pressure difference of ≈1 kPa between the capillary tip and the moving droplets. The small size of the capillary ensures that a high pressure difference is achieved, which prevents secondary droplets from forming at the injector over a relatively wide range of flow rates. A higher pressure difference leads to

a larger flow rate during injection, and thus a larger injection volume. Therefore, Equation (1) also shows that the injection volume can be extended by using a smaller capillary or higher interfacial tension. Figure 2c shows an optical micrograph of a droplet passing through the Venturi junction, where the boundaries of the droplets are highlighted with red dashed lines. Good contact with the capillary can be observed.

Finally, the higher pressure in the side channel as compared with the main channel ensures that no cross-contamination occurs between the droplet and the side channel, and that any precipitants generated during injection are entirely transferred to the droplet. This is demonstrated by injecting Millipore water into a droplet containing fluorescent dye, as shown in Figure 2d. Our picoinjector design therefore effectively avoids any problems of channel fouling in crystallization studies—even for rapidly-precipitated compounds.

2.3. Control of Injection Volume

Our device also enables excellent control over the volume injected into the droplets, where this is achieved by varying the flow rate of the injection solution. This is illustrated in **Figure 3**, where the data shown were collected from over 200 droplets in a single experiment, and the experiments were performed three times. Flow rates of 6 and 0.5 μL min^{-1} were applied to the carrier oil (FC-40) and water for droplet generation, respectively, while the flow rate in the capillary was varied between 0.1 and 0.6 μL min^{-1}. The data demonstrate an almost linear relation between the capillary flow rate and injection volume, where volumes of 0.2 to 1.4 nL were injected into 1.4 nL droplets in this device. Capillary flow rates of above 0.6 μL min^{-1} resulted in the formation of secondary droplets at the capillary tip rather than injection, such that an upper limit of 0.5 μL min^{-1} was employed. Selected images of a droplet just prior to, and just after injection, are also shown on the upper left of Figure 3, while images of droplets collected at the device outlet are shown on the lower right of the figure. These images confirm the integrity of the droplets after injection, and show that the size of the droplet and intensity of the blue dye increases with the volume injected.

The injection volume also depends on the residence time of the flowing droplet at the injector. An increase in the flow rate of the first aqueous solution at the "Y-junction" will generate larger droplets, and thus a larger injection volume due to the increase of residence time. Conversely, an increase of flow rate of the oil will give rise to a smaller injection volume due to the smaller droplet size and corresponding shorter residence time. As a demonstration of the ability to control the injection volume, the flow rate of the oil and first aqueous solution were kept constant and the flow rate of the injection solution was varied. A video of the injection process is supplied as Movie S1 (Supporting Information), and the formation of secondary droplets at high flow rates in Movie S2 (Supporting Information).

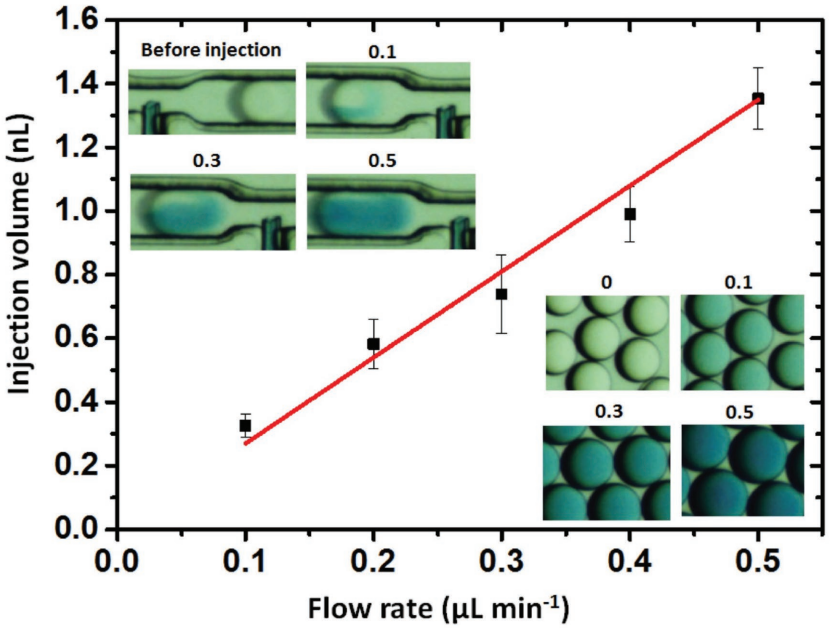

Figure 3. Graph showing how the injection volume can be controlled according to the flow rate of solution (here dyed blue) in the side channel. The upper-left images provide snapshots after injection, while the lower-right images show isolated droplets after injection. The numbers accompanying the images indicate the flow rate of fluid in the side channels with units of μL min^{-1}.

2.4. Precipitation of Calcium Carbonate

Having developed an easy-to-use picoinjector, we then explored the impact of different elements of the device design on crystallization. SEM and Raman microscopy were used throughout to distinguish the different polymorphs of the calcium carbonate crystals. ACC appears as spherical nanoparticles, and its Raman spectrum exhibits a broad peak at 1084 cm^{-1} (ν_1), and there is a notable absence of the ν_4 peak around 700 cm^{-1}.[30] Vaterite typically appears as polycrystalline, micrometer-scale spherical particles and in Raman exhibits a double peak at 1092 and 1076 cm^{-1} (ν_1) and other peaks at 752 cm^{-1} (ν_4) and 299 cm^{-1}.[30] Calcite precipitates as well-defined rhombohedra, and exhibits peaks at 1086 cm^{-1} (ν_1), 712 cm^{-1} (ν_4), and 274 and 150 cm^{-1}.[30] Typical Raman spectra and Scanning Electron Microscope (SEM) images of ACC, vaterite, and calcite generated in this study are shown in **Figure 4**. The additional peaks seen in the Raman spectra correspond to the background track-etched membrane.

2.5. Role of Effective Mixing

The impact of the rate of mixing in the microdroplets on the crystallization process was investigated by comparing devices which were otherwise identical, but which exhibited either straight or serpentine channels in the zone after the picoinjector. **Figures 5**a,c show images recorded after injecting blue dye into moving water droplets in both chips. It is

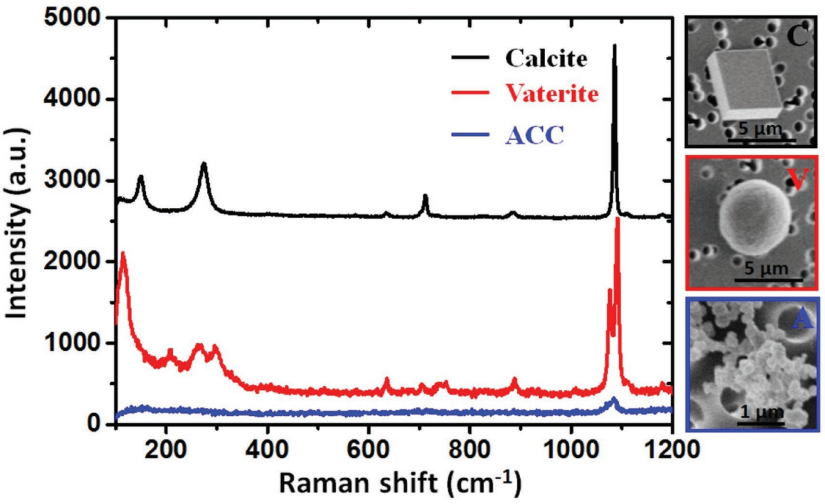

Figure 4. Representative Raman spectra and the corresponding SEM images of ACC (blue), vaterite (red), and calcite (black) generated in microfluidic devices in this study, where C, V, and A represent calcite, vaterite, and ACC, respectively. The background of porous material in the SEM images is the track-etched membrane used to collect crystals from droplets by vacuum filtration.

clearly seen that the droplet is thoroughly mixed in the serpentine channel, but that mixing is slower in the straight channel. $CaCO_3$ was precipitated in these two devices, where conditions of $[Ca^{2+}] = [CO_3^{2-}] = 2.5 \times 10^{-3}$ M were created by combining equal volumes of 5×10^{-3} M cation and anion solutions, and crystals were collected 5 min after picoinjection by vacuum filtration through a track-etched membrane.

Figures 5b,d show SEM images of the crystals obtained from the microfluidic chips with straight and serpentine channels. Effective, early-time mixing can be seen to have a significant effect on polymorph production, where the straight channel device delivers a population of vaterite particles, together with some calcite rhombohedra (Figure 5b). The serpentine channel device, in contrast, produces rhombohedral calcite crystals, together with a few vaterite particles (Figure 5d). These data were also compared with bulk crystallization experiments in which equal volumes of 5×10^{-3} M $CaCl_2$ and Na_2CO_3 solutions were combined in a 1.5 mL centrifuge tube, and crystals were collected after 5 min. The crystals generated were >99% calcite (Figure S1, Supporting Information), in good agreement with the serpentine channel mixing. The provision of effective mixing is therefore essential in droplet crystallization and a serpentine channel could be regarded as standard in the device design.

2.6. Crystallization at High Supersaturations

While a significant body of work exists on the precipitation of proteins within microfluidic devices, the precipitation of insoluble compounds such as $CaCO_3$ in segmented flow systems

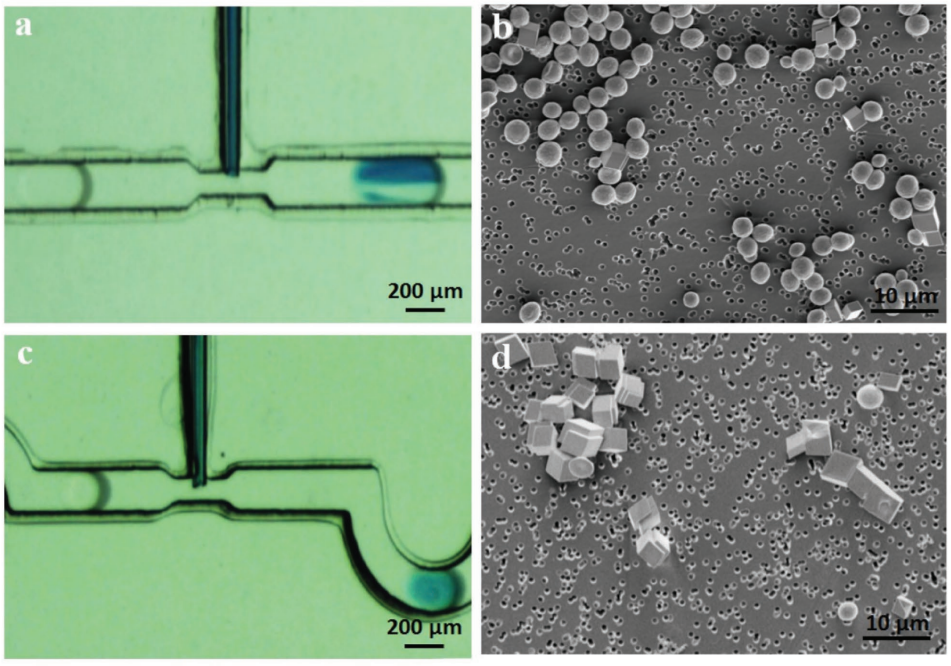

Figure 5. Snapshots of microdroplets in a straight channel a) and in a serpentine channel c) just after injection of blue color dye into moving droplets. The flow rates of carrier oil (FC-40), water, and dye were kept at 6, 0.5, and 0.3 µL min^{-1}, respectively. b,d) The corresponding SEM images of crystallization products for straight channel and serpentine channel under the condition of $[Ca^{2+}] = [CO_3^{2-}] = 2.5 \times 10^{-3}$ M. The crystals were collected after 5 min when $CaCl_2$ and Na_2CO_3 are combined by injection with 1:1 volume ratio.

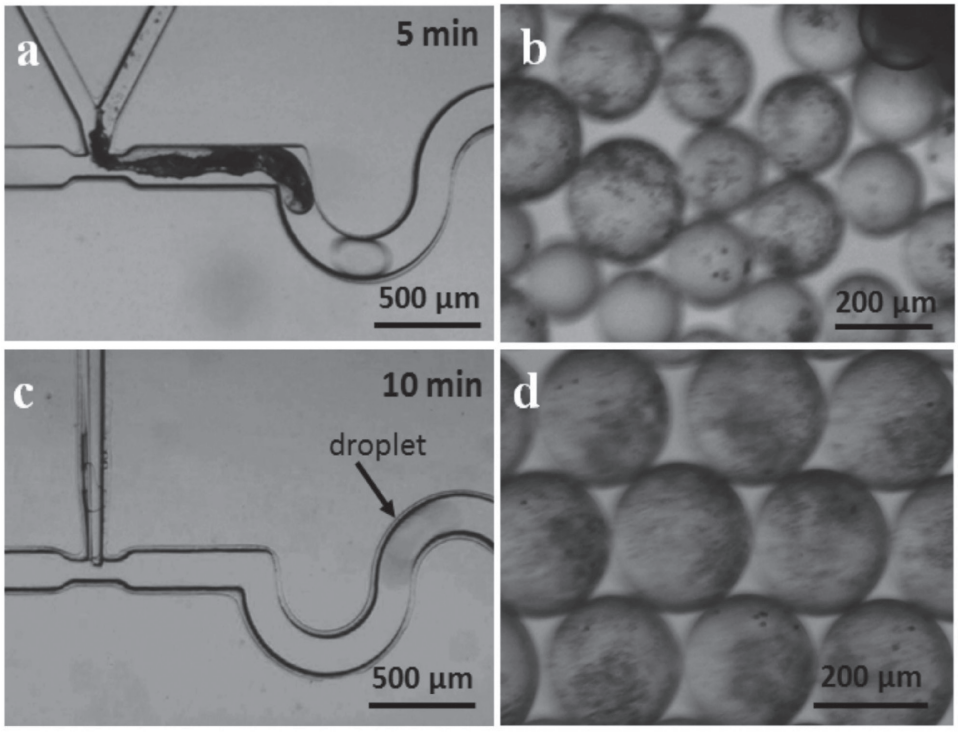

Figure 6. Optical microscope images of $CaCO_3$ precipitation in droplets ($[Ca^{2+}] = [CO_3^{2-}] = 50 \times 10^{-3}$ M) a) after 5 min when anion and cation solutions are combined using a Y-channel, and c) after 10 min when the anion and cation solutions are combined using the picoinjector. b,d) Images of the droplets collected in (a) and (c), respectively.

creates additional challenges as they rapidly precipitate from low concentration solutions. Uncontrolled precipitation thus readily occurs at the point of droplet formation, resulting in device blocking and the transfer of preformed crystals into droplets, which necessarily alters the crystallization process. We therefore compared the operation of our device under high and low supersaturation conditions, where the supersaturation index (SI)[31] is defined as $\log\sigma = \log(a_{Ca^{2+}} \cdot a_{CO_3^{2-}}/K_{sp})$ and was calculated using Visual Minteq (see the Experimental section).

Considering first high supersaturation solutions, $CaCO_3$ was precipitated by combining equimolar $CaCl_2$ and Na_2CO_3 solutions at a Y-junction immediately prior to droplet formation to give a final concentration of $[Ca^{2+}] = [CO_3^{2-}] = 50 \times 10^{-3}$ M and SI (wrt ACC) of 3.21 and 4.56 wrt calcite. ACC therefore immediately precipitates on combination of these solutions. **Figure 6**a shows an optical microscope image of the device after a run-time of 5 min, at which point there is a significant quantity of precipitated $CaCO_3$ in one of the channels. This causes a nonuniform population of droplets to form and these preprecipitated $CaCO_3$ particles become entrapped within droplets (Figure 6b). Raman microscopy was used to identify these particle aggregates as ACC (Figure S2, Supporting Information). It is therefore not possible to use this device design to reproducibly study the de novo precipitation of $CaCO_3$ at high supersaturation within flowing droplets.

Identical supersaturation conditions were also employed to perform intradroplet precipitation of $CaCO_3$ using direct injection. In detail, 100×10^{-3} M $CaCl_2$ droplets were generated at the T-junction and identical volumes of 100×10^{-3} M Na_2CO_3 were injected into each droplet at the Venturi junction. The channels remain completely free of precipitates after a run-time of 10 min (Figure 6c), and a highly uniform population of droplets is formed (Figure 6d). Examination of the precipitation pathway in this system shows that significant precipitation of ACC occurs within milliseconds of injection of the carbonate solution into the droplet (Movie S3, Supporting Information), where the polymorph was confirmed using Raman spectroscopy.

The droplets were then collected at the outlet of the device and were imaged over time using an optical microscope (**Figure 7**). Crystalline particles were seen in 64% of droplets within 30 mins, as confirmed by polarized light microscopy, where they grow at the expense of the ACC. This is consistent with a dissolution-reprecipitation mechanism as is expected for ACC in solution.[32] The product crystalline particles were also characterized using SEM and Raman microscopy, and after 2.5 h the principal polymorphs present were calcite and vaterite (in approximately equal amounts), together with small amounts of ACC (Figure S3, Supporting Information). These polymorph assignments were confirmed by Raman. Notably, while the ACC begins to crystallise within 2 h in the vast majority of droplets, some (≈14%) show no evidence of crystallization, even after 2.5 h. This compares with bulk solutions of the same supersaturation where crystallization is complete after 40 min, yielding ≈2% calcite and 98% vaterite (Figure S4, Supporting Information).

That crystallization proceeds more slowly in the droplets than in bulk solution and is fully consistent with studies of the

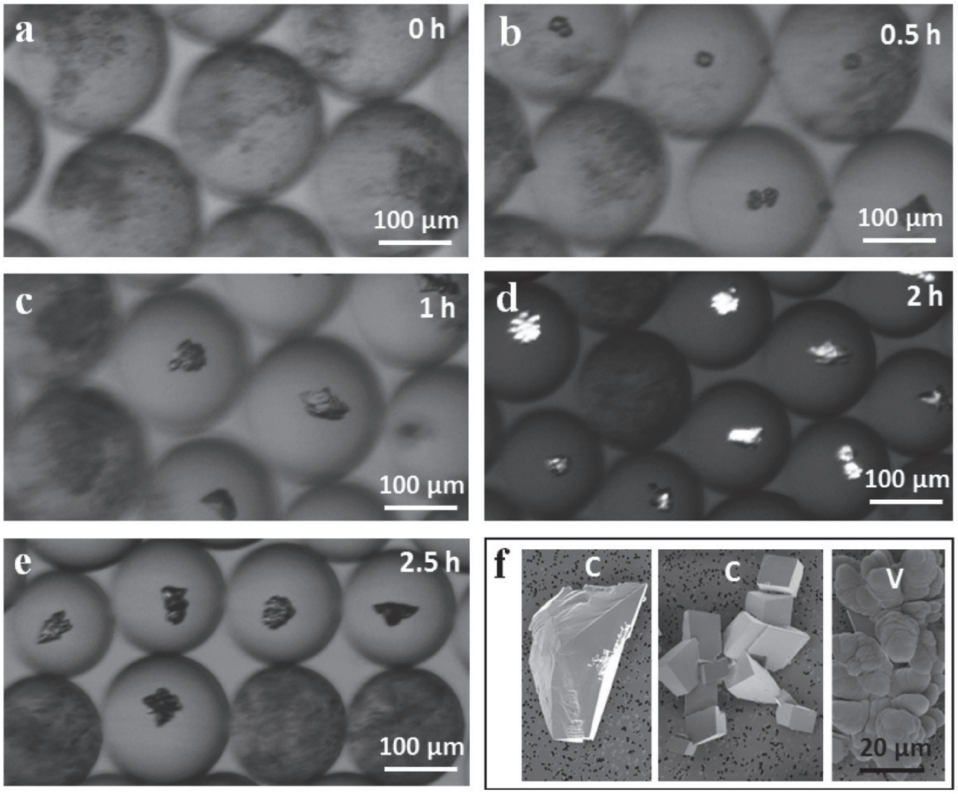

Figure 7. a–e) Optical microscope images of $CaCO_3$ precipitation in droplets after different incubation times. Crystallization was induced by picoinjection to give droplet concentrations of $[Ca^{2+}] = [CO_3^{2-}] = 50 \times 10^{-3}$ M and d) was recorded using crossed polarisers. f) SEM image of crystals collected after 2.5 h (C: calcite and V: vaterite).

effects of confinement on crystallization, which show that crystallization proceeds more slowly in small volumes, such that metastable phases are longer lived.[33] Although the origins of this effect are not entirely clear, the exclusion of impurities from droplets, the elimination of convection effects, and the reduction in competition effects are all likely to play a role.[34] The results also suggest that nucleation is suppressed in the droplets.

2.7. Crystallization at Low Supersaturations

$CaCO_3$ precipitation from solutions of lower supersaturation gives rise to significantly less precipitation in the Y-channel, and reproducible droplet generation was achieved from solutions with final concentrations of $[Ca^{2+}] = [CO_3^{2-}] = 2.5 \times 10^{-3}$ M (SI = 0.94 wrt ACC and 2.27 wrt calcite) after 20 min. However, significant differences were observed in the crystallization products generated at this supersaturation by Y-channel loading and direct injection experiments at times 0 and 10 min after initiation of flow. In each case droplets were collected for 2 min and were then incubated for 5 min prior to isolation of the $CaCO_3$ particles. **Figure 8**a–d shows images of the crystals isolated and demonstrates that when the Y-channel method is employed, the sizes and polymorphs of the particles differ at 0 (Figure 8a) and 10 min (Figure 8b). While the population of crystals comprise almost equal numbers of 5 µm calcite and 3 µm vaterite at 0 min, they are almost exclusively 2 µm vaterite after 10 min. The direct injection method, in contrast, delivers consistent results, where the products at 0 and 10 min both comprise 5 µm vaterite and 8 µm calcite particles (in a 1:5 ratio, Figure 8c,d). Additional SEM pictures are shown in Figures S5–S8 (Supporting Information).

The origin of the inconsistency in the results from the Y-junction device was investigated by examining the inside of the chip after the device had been run for 10 min. Multiple calcium carbonate particles can be seen on the PDMS surface of the Y-shape channel using SEM (Figure 8e). The majority of the particles are spherical in shape and were identified as vaterite using Raman microscopy, while the remaining particles are rhombohedral calcite (Figure S9, Supporting Information). The presence of these particles will influence crystallization within the droplets, where their growth will deplete the concentration of the solution forming the droplets, or many could be transferred to the droplets as they are formed (perhaps at smaller sizes), where they subsequently act as seeds. Therefore, although this level of in-channel precipitation does not interfere with droplet generation, it is significant enough to affect the crystallization process.

3. Discussion

Segmented-flow microfluidic devices have enormous potential for the study of crystallization processes. The ability to

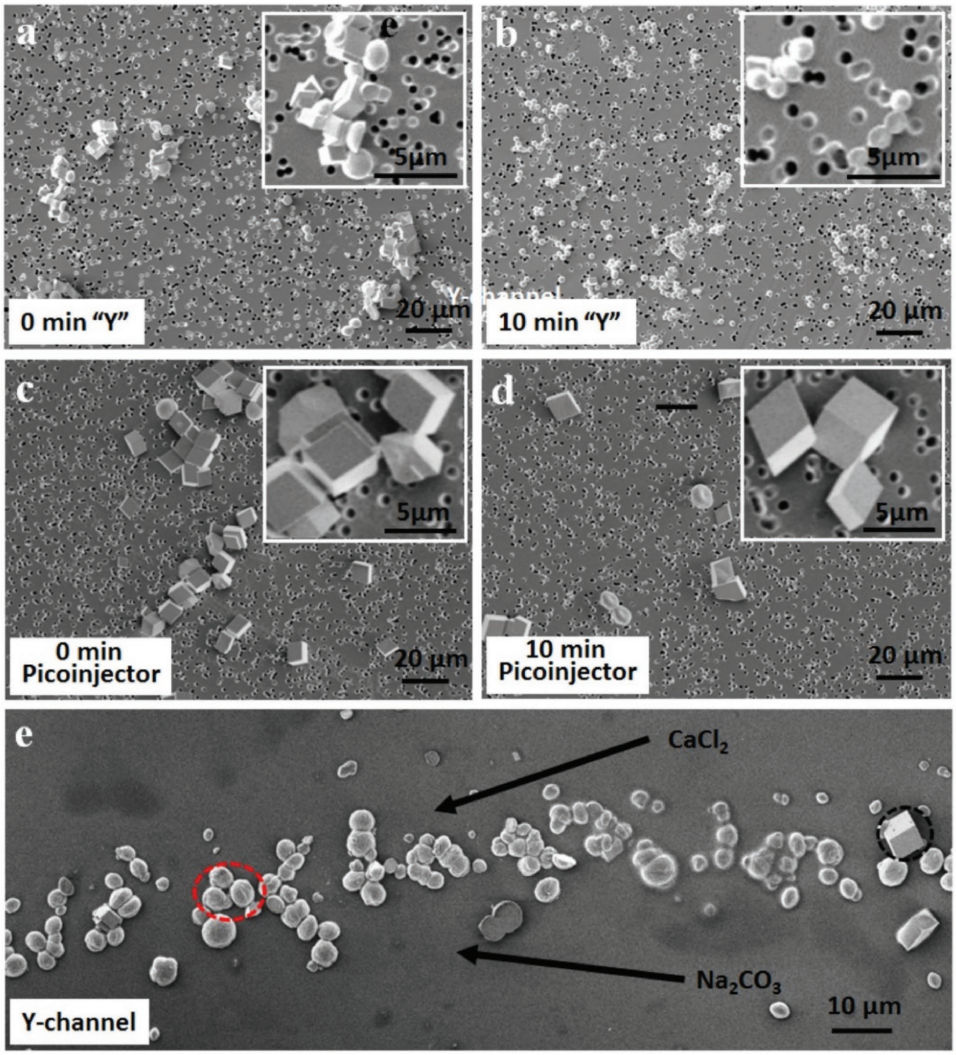

Figure 8. SEM images of $CaCO_3$ crystals produced by a,b) Y-channel loading and c,d) picoinjection, where droplet collection was started at chip runtimes of 0 and 10 min. In each case droplets were collected over a 2 min time-frame and the crystals were isolated after an incubation time of 5 min. The concentration in the droplets was $[Ca^{2+}] = [CO_3^{2-}] = 2.5 \times 10^{-3}$ M. e) SEM image of crystals absorbed on the surface of the Y-channel after running the chip for 10 min. The vaterite and calcite crystals are highlighted with red and black circles. The black arrows indicate the flow directions of the $CaCl_2$ and Na_2CO_3 solutions in the Y-channel.

achieve rapid mixing of reagents and to facilitate analysis with millisecond time resolution[35,36] makes them ideally suited to the study of rapid processes, and in particular the early stages of precipitation at high supersaturations. On-chip analysis can be conducted using a wide range of techniques including Raman spectroscopy and small and wide angle X-ray scattering.[3,37] Importantly, as a major distinction from the analysis of static samples, the screening time of an individual droplet is extremely short, and data are recorded as a summation over a large number of identical droplets. The effect of the analysis process on the reaction being studied is therefore minimized or eliminated, where this can be a problem when high energy techniques such as synchrotron-based methods[38] or liquid-cell Transmission electron microscopy (TEM)[39] are used to investigate static samples.

Using microfluidic devices to study crystallization processes of course also depends on the chip being able to operate reliably for extended periods of time, where this is particularly important, for example, if setting up a chip for synchrotron analysis. As demonstrated here, a significant hurdle to the use of microfluidic devices for studying the precipitation of insoluble materials is nonspecific precipitation. This can be overcome by using droplet fusion techniques, where a stream comprising an alternating sequence of droplets is created, and then pairs of droplets are fused. However, it is difficult to achieve reliable fusion over extended periods.[23] Direct injection into flowing droplets is potentially more flexible and a range of methods have been explored to achieve this goal. At the most simple, single, and multiple Y-junctions have been used to add solution to surfactant-free plugs during protein crystallization.[17,40] However, problems with cross-contamination and nonspecific

precipitation can occur using this approach, which can be severe for highly insoluble materials.

The "picoinjector" offers a more sophisticated method of direct injection[21] and enables controlled volumes to be added to surfactant-stabilized droplets; the short contact time avoids problems of channel fouling. However, standard designs of picoinjectors require an electric field to break the surface tension of the droplet[24] and thus achieve injection. This can be achieved by integrating electrodes into the chip, which makes picoinjection chips complex to construct. Some simplification has been achieved using the injection fluid as an electrode,[41] such that integrated electrodes are not required. There is therefore a recognized need for reliable and easy-to-use direct injection methods that can be operated in the absence of applied electric fields, where a notable example was designed around a three-phase flow reactor in which reagents are injected into a multiphase fluid stream comprising the carrier liquid, droplets of the reaction mixture, and an inert gas.[22] Our novel design of picoinjector therefore achieves this target, where integration of a simple Venturi junction facilitates direct injection into surfactant-stabilized droplets in the absence of an applied electric field.

4. Conclusions

This article describes a novel microfluidic device which opens the door to studying the precipitation of insoluble crystals over extended periods of operation. Importantly, the chip design is sufficiently simple and easy-to-use that it can be employed by crystallization research groups rather than specialist microfluidic labs. As demonstrated for the precipitation of calcium carbonate from highly supersaturated solutions, our device offers excellent reproducibility due to the elimination of nonspecific crystallization at, or prior to, droplet formation. Central to our strategy is the use of picoinjection to generate droplets of supersaturated solution, where this eliminates all problems of nonspecific precipitation. This is achieved using a new design of picoinjector which employs a Venturi junction to reduce the pressure within the droplet at the point of injection, therefore enabling injection into surfactant-stabilized droplets. Further, precise control over the injection volume can be readily achieved by varying the flow rate in the injection capillary. Our picoinjector is therefore simple to implement, since no external sources such as electronic instruments, ultrasonic probes, or lasers are required for injection. Although demonstrated for the study of crystallization reactions, this picoinjector design can be employed in any application requiring precise control over injection volumes, including preforming multistep chemical reactions without cross-contamination, and the investigation of reaction dynamics.

5. Experimental Section

Fabrication of Microfluidic Devices: Microfluidic devices were fabricated from PDMS using soft photolithographic techniques. Quartz capillaries (World Precision Instruments) were pulled using a laser pipette puller (P2000, Sutter Instruments) with a single step program: (1) HEAT: 700; FIL: 4; VEL: 60; DEL: 145; PUL: 175. The capillary was then cut into a short section at distances 6 and 8 mm from the tip (Figure 1b), and the section was placed in the PDMS side channel.

Simulation of Fluid Flow through Venturi Junction: The Venturi effect was simulated using COMSOL Multiphysics 4.2 (Comsol, Inc.) using a single phase laminar flow model with 2D stationary setting. The physical properties of flowing fluid were set those of FC-40 (density: 1855 kg m^{-3}, dynamic viscosity: 2.5 mPa s).

Solution Preparation and Device Operation: A 10 vol% solution of blue food colouring (Knightsbridge PME Ltd.) in Millipore water was used for injection volume calibration, while a 1 mg mL^{-1} solution of the fluorescent dye, 8-hydroxypyrene-1,3,6-trisulfonic acid trisodium salt (Sigma-Aldrich), was used to monitor the injection process. Droplets were suspended in a carrier oil of FC-40 fluorinated oil (Sigma) containing 0.5% (wt/wt) raindance surfactant,[42] while $CaCl_2$ and Na_2CO_3 solutions were prepared in Millipore water. The aqueous solutions and carrier oil were introduced into the microfluidic chips using Cetoni Nemesys syringe pumps, and optical images and movies were recorded using a Zeiss Stereo Discovery V8, an M165FC Microscope (Leica) and a Zeiss Axio Imager Z1 optical microscope equipped with a Phantom micro 310 high speed camera (Vision Research Ltd., USA).

Crystallization in Bulk Solution: $CaCO_3$ was also precipitated in bulk solution in order to compare the crystallization products with those generated in droplets. Equal volumes (200 µL) of 5×10^{-3} M $CaCl_2$ and 5×10^{-3} M Na_2CO_3 solutions were combined in a 1.5 mL centrifuge tube and crystals were collected after 5 min by filtration through a track-etched membrane with 800 nm pores. Crystallization at high supersaturation was performed in the similar way by combining 200 µL volumes of 100×10^{-3} M $CaCl_2$ and Na_2CO_3 solutions in a centrifuge tube, followed by vacuum filtration after 40 min to isolate crystals.

Material Characterization: $CaCO_3$ crystals were isolated from droplets using vacuum filtration on a track etched membrane with pores of size 0.8 µm (Millipore), followed by washing with ethanol. SEM images of iridium-coated samples were recorded using an FEI Nova NanoSEM operating at 3 kV. Analysis of crystal polymorphs was carried out by Raman microscopy using a Renishaw In-Via system with 785 nm laser.

Calculation of Supersaturation: The supersaturation levels of the reaction solutions employed were estimated using Visual MINTEQ version 3.1 (KTH, Sweden). The SI is defined as $\log\sigma = \log(a_{Ca^{2+}} \cdot a_{CO_3^{2-}}/K_{sp})$, where this was calculated with respect to ACC ($K_{sp,acc} = 10^{-6.393}$), vaterite ($K_{sp,vaterite} = 10^{-7.93}$), or calcite ($K_{sp,calcite} = 10^{-8.48}$) for a temperature of 25 °C.

Supporting Information

Supporting Information is available from the Wiley Online Library or from the author.

Acknowledgements

The authors thank the financial support by the Engineering and Physical Sciences Research Council (EPSRC) under grants EP/L015005/1 (S.L., T.G., M.J.M., and F.C.M.) and EP/N002423/1 (F.C.M. and M.Z.). In keeping with EPSRC policy, the dataset associated with this article can be accessed at https://doi.org/10.5518/234.

Conflict of Interest

The authors declare no conflict of interest.

Keywords

calcium carbonate, crystallization, device fouling, microfluidics, picoinjector

Received: June 25, 2017
Published online: September 5, 2017

[1] a) H. Song, D. L. Chen, R. F. Ismagilov, *Angew. Chem. Int. Ed.* **2006**, *45*, 7336; b) J. Puigmarti-Luis, *Chem. Soc. Rev.* **2014**, *43*, 2253; c) J. Leng, J.-B. Salmon, *Lab Chip* **2009**, *9*, 24; d) T. Y. Nguyen, E. A. Roessler, K. Rademann, F. Emmerling, *Z. Kristallogr. — Cryst. Mater.* **2017**, *232*, 15.
[2] J. Dai, H. S. Kim, A. R. Guzman, W.-B. Shim, A. Han, *RSC Adv.* **2016**, *6*, 20516.
[3] Y. Zhu, Q. Fang, *Anal. Chim. Acta* **2013**, *787*, 24.
[4] S. Li, J. Ihli, W. J. Marchant, M. Zeng, L. Chen, K. Wehbe, G. Cinque, O. Cespedes, N. Kapur, F. C. Meldrum, *Lab Chip* **2017**, *17*, 1616.
[5] a) P. Laval, A. Crombez, J.-B. Salmon, *Langmuir* **2009**, *25*, 1836; b) T. A. Prileszky, E. M. Furst, *Langmuir* **2016**, *32*, 5141; c) J. Lu, J. D. Litster, Z. K. Nagy, *Cryst. Growth Des.* **2015**, *15*, 3645; d) S. V. Akella, A. Mowitz, M. Heymann, S. Fraden, *Cryst. Growth Des.* **2014**, *14*, 4487.
[6] M. Ildefonso, N. Candoni, S. Veesler, *Cryst. Growth Des.* **2011**, *11*, 1527.
[7] a) M. Maeki, H. Yamaguchi, M. Tokeshi, M. Miyazaki, *Anal. Sci.* **2016**, *32*, 3; b) M. Ildefonso, E. Revalor, P. Punniam, J. B. Salmon, N. Candoni, S. Veesler, *J. Cryst. Growth* **2012**, *342*, 9.
[8] H. Yamaguchi, M. Maeki, K. Yamashita, H. Nakamura, M. Miyazaki, H. Maeda, *J. Biochem.* **2013**, *153*, 339.
[9] L. Li, R. F. Ismagilov, *Ann. Rev. Biophys.*, **2010**, *39*, 139.
[10] a) T. Tokuhisa, M. Kawasaki, D. Kisailus, M. Yuda, T. Matsunaga, A. Arakaki, *Cryst. Growth Des.* **2015**, *15*, 4549; b) R. A. L. Leon, A. Z. M. Badruddoza, L. Zheng, E. W. Q. Yeap, A. I. Toldy, K. Y. Wong, T. A. Hatton, S. A. Khan, *Cryst. Growth Des.* **2015**, *15*, 212.
[11] N. Jiang, Z. Z. Wang, L. P. Dang, H. Y. Wei, *J. Cryst. Growth* **2016**, *446*, 68.
[12] A. Yashina, F. Meldrum, A. Demello, *Biomicrofluidics* **2012**, *6*, 22001.
[13] P. Laval, C. Giroux, J. Leng, J. B. Salmon, *J. Cryst. Growth* **2008**, *310*, 3121.
[14] a) J. F. Edd, K. J. Humphry, D. Irimia, D. A. Weitz, M. Toner, *Lab Chip* **2009**, *9*, 1859; b) X. Gong, Y.-W. Wang, J. Ihli, Y.-Y. Kim, S. Li, R. Walshaw, L. Chen, F. C. Meldrum, *Adv. Mater.* **2015**, *27*, 7395.
[15] a) B. Zheng, J. D. Tice, L. S. Roach, R. F. Ismagilov, *Angew. Chem. Int. Ed.* **2004**, *43*, 2508; b) J. U. Shim, G. Cristobal, D. R. Link, T. Thorsen, Y. W. Jia, K. Piattelli, S. Fraden, *J. Am. Chem. Soc.* **2007**, *129*, 8825.
[16] a) C. Sauter, K. Dhouib, B. Lorber, *Cryst. Growth Des.* **2007**, *7*, 2247; b) S. L. Perry, S. Guha, A. S. Pawate, A. Bhaskarla, V. Agarwal, S. K. Nair, P. J. A. Kenis, *Lab Chip* **2013**, *13*, 3183.
[17] C. J. Gerdts, V. Tereshko, M. K. Yadav, I. Dementieva, F. Collart, A. Joachimiak, R. C. Stevens, P. Kuhn, A. Kossiakoff, R. F. Ismagilov, *Angew. Chem. Int. Ed.* **2006**, *45*, 8156.
[18] A. I. Toldy, A. Z. M. Badruddoza, L. Zheng, T. A. Hatton, R. Gunawan, R. Rajagopalan, S. A. Khan, *Cryst. Growth Des.* **2012**, *12*, 3977.
[19] a) M. Schoenitz, L. Grundemann, W. Augustin, S. Scholl, *Chem. Commun.* **2015**, *51*, 8213; b) H. B. Yin, B. Z. Ji, P. S. Dobson, K. Mosbahi, A. Glidle, N. Gadegaard, A. Freer, J. M. Cooper, M. Cusack, *Anal. Chem.* **2009**, *81*, 473.
[20] L. Frenz, A. El Harrak, M. Pauly, S. Begin-Colin, A. D. Griffiths, J. C. Baret, *Angew. Chem. Int. Ed.* **2008**, *47*, 6817.
[21] A. R. Abate, T. Hung, P. Mary, J. J. Agresti, D. A. Weitz, *Proc. Natl. Acad. Sci. USA* **2010**, *107*, 19163.
[22] A. M. Nightingale, T. W. Phillips, J. H. Bannock, J. C. de Mello, *Nat. Commun.* **2014**, *5*, 3777.
[23] M. Lee, J. W. Collins, D. M. Aubrecht, R. A. Sperling, L. Solomon, J. W. Ha, G. R. Yi, D. A. Weitz, V. N. Manoharan, *Lab Chip* **2014**, *14*, 509.
[24] a) S. L. Sjostrom, H. N. Joensson, H. A. Svahn, *Lab Chip* **2013**, *13*, 1754; b) M. Rhee, Y. K. Light, S. Yilmaz, P. D. Adams, D. Saxena, R. J. Meagher, A. K. Singh, *Lab Chip* **2014**, *14*, 4533; c) E. X. Ng, M. A. Miller, T. Jing, D. A. Lauffenburger, C. H. Chen, *Lab Chip* **2015**, *15*, 1153.
[25] a) F. C. Meldrum, *Int. Mater. Rev.* **2003**, *48*, 187; b) F. C. Meldrum, H. Colfen, *Chem. Rev.* **2008**, *108*, 4332.
[26] a) L. Jiang, Y. Zeng, H. Zhou, J. Y. Qu, S. Yao, *Biomicrofluidics* **2012**, *6*, 12810; b) J. Dai, X. Yang, M. Hamon, L. Kong, *Chem. Eng. J.* **2015**, *280*, 385.
[27] S. Li, M. Li, Y. S. Hui, W. Cao, W. Li, W. Wen, *Microfluid. Nanofluid.* **2012**, *14*, 499.
[28] D. S. Chang, S. M. Langelier, M. A. Burns, *Lab Chip* **2007**, *7*, 1791.
[29] L. Mazutis, A. D. Griffiths, *Lab Chip* **2012**, *12*, 1800.
[30] a) M. M. Tlili, M. Ben Amor, C. Gabrielli, S. Joiret, G. Maurin, P. Rousseau, *J. Raman Spectrosc.* **2002**, *33*, 10; b) E. H. Noel, Y.-Y. Kim, J. M. Charnock, F. C. Meldrum, *Crystengcomm* **2013**, *15*, 697.
[31] a) Y. S. Han, G. Hadiko, M. Fuji, M. Takahashi, *J. Cryst. Growth* **2005**, *276*, 541; b) W. Sun, S. Jayaraman, W. Chen, K. A. Persson, G. Ceder, *Proc. Natl. Acad. Sci. USA* **2015**, *112*, 3199.
[32] a) K. Sawada, *Pure Appl. Chem.* **1997**, *69*, 921; b) J. Ihli, W. C. Wong, E. H. Noel, Y. Y. Kim, A. N. Kulak, H. K. Christenson, M. J. Duer, F. C. Meldrum, *Nat. Commun.* **2014**, *5*, 3169; c) J. Ihli, Y.-Y. Kim, E. H. Noel, F. C. Meldrum, *Adv. Funct. Mater.* **2013**, *23*, 1575.
[33] a) C. C. Tester, M. L. Whittaker, D. Joester, *Chem. Commun.* **2014**, *50*, 5619; b) B. Cantaert, E. Beniash, F. C. Meldrum, *Chem. — Eur. J.* **2013**, *19*, 14918; c) Y.-Y. Kim, N. B. J. Hetherington, E. H. Noel, R. Kroeger, J. M. Charnock, H. K. Christenson, F. C. Meldrum, *Angew. Chem. Int. Ed.* **2011**, *50*, 12572; d) C. Anduix-Canto, Y.-Y. Kim, Y.-W. Wang, A. Kulak, F. C. Meldrum, H. K. Christenson, *Cryst. Growth Des.* **2016**, *16*, 5403; e) C. C. Tester, R. E. Brock, C.-H. Wu, M. R. Krejci, S. Weigand, D. Joester, *CrystEngComm* **2011**, *13*, 3975.
[34] a) C. J. Stephens, S. F. Ladden, F. C. Meldrum, H. K. Christenson, *Adv. Funct. Mater.* **2010**, *20*, 2108; b) Y.-W. Wang, H. K. Christenson, F. C. Meldrum, *Chem. Mater.* **2014**, *26*, 5830; c) Y.-W. Wang, H. K. Christenson, F. C. Meldrum, *Adv. Funct. Mater.* **2013**, *23*, 5615; d) C. J. Stephens, Y.-Y. Kim, S. D. Evans, F. C. Meldrum, H. K. Christenson, *J. Am. Chem. Soc.* **2011**, *133*, 5210.
[35] V. S. Cabeza, S. Kuhn, A. A. Kulkarni, K. F. Jensen, *Langmuir* **2012**, *28*, 7007.
[36] I. Lignos, S. Stavrakis, A. Kilaj, A. J. deMello, *Small* **2015**, *11*, 4009.
[37] A. Ghazal, J. P. Lafleur, K. Mortensen, J. P. Kutter, L. Arleth, G. V. Jensen, *Lab Chip* **2016**, *16*, 4263.
[38] P. Bots, L. G. Benning, J. D. Rodriguez-Blanco, T. Roncal-Herrero, S. Shaw, *Cryst. Growth Des.* **2012**, *12*, 3806.
[39] J. J. De Yoreo, N. Sommerdijk, *Nat. Rev. Mater.* **2016**, *1*, 18.
[40] L. Li, J. Q. Boedicker, R. F. Ismagilov, *Anal. Chem.* **2007**, *79*, 2756.
[41] B. O'Donovan, D. J. Eastburn, A. R. Abate, *Lab Chip* **2012**, *12*, 4029.
[42] C. Holtze, A. C. Rowat, J. J. Agresti, J. B. Hutchison, F. E. Angile, C. H. Schmitz, S. Koster, H. Duan, K. J. Humphry, R. A. Scanga, J. S. Johnson, D. Pisignano, D. A. Weitz, *Lab Chip* **2008**, *8*, 1632.